Rare Metals

WILEY | 有科出版 YOUKE PUBLISHING

ORIGINAL ARTICLE OPEN ACCESS

Interfacial Reconstruction of Li^+ Solvation Shell for Fast Diffusion Kinetics in Low-Temperature Dendrite-Free Li Metal Battery Enabled by Atomic Catalysts

Shikai Yin[1] | Jing Zhang[1] | Mannan Yang[1] | Yang Hu[2,3] | Bixian Chen[4] | Na Tian[1] | Hao Li[2,3] | Caiyin You[1] | Dongmao Jiao[1] | Zhenjiang Cao[5] | Yongzheng Zhang[6] | Lin Li[1] | Dong Wang[7] | Hongzhen Lin[4] | Jian Wang[2,3]

[1]School of Materials Science and Engineering & Packaging Engineering and Digital Media Technology, Xi'an University of Technology, Xi'an, China | [2]Helmholtz Institute Ulm (HIU), Ulm, Germany | [3]Karlsruhe Institute of Technology (KIT), Karlsruhe, Germany | [4]i-Lab & CAS Key Laboratory of Nanophotonic Materials and Devices, Suzhou Institute of Nano-Tech and Nano-Bionics, Chinese Academy of Sciences, Suzhou, China | [5]School of Chemistry, Engineering Research Center of Energy Storage Materials and Devices, Xi'an Jiaotong University, Xi'an, China | [6]School of Textile & Clothing, Nantong University, Nantong, China | [7]School of Materials Science & Engineering and International Center of Future Science, Jilin University, Changchun, China

Correspondence: Jing Zhang (zhangjing2020@xaut.edu.cn) | Na Tian (tianna@xaut.edu.cn) | Jian Wang (jian.wang@kit.edu; wangjian2014@sinano.ac.cn)

Received: 25 February 2026 | **Revised:** 9 April 2026 | **Accepted:** 11 April 2026

Keywords: dendrite inhibition | desolvation modulation | electron-delocalization catalysis | low-temperature Li metal battery | solvation reconstruction

ABSTRACT

Low-temperature lithium-metal batteries (LT-LMBs) are increasingly pursued for higher energy density and extended cycle life, yet suffer from severely depressed interfacial Li^+ desolvation/diffusion kinetics due to the enlarged solvation structures as well as organic electrolyte solidification, ultimately inducing much higher barriers to overcome. Herein, the interfacial structure of the Li^+ solvation shell has been remodeled for fast diffusion kinetics in low-temperature surroundings via an atomic catalyst. Briefly, the interfacial electron-delocalization catalysis engineered by anchoring single-atomic Zn into defect-rich vanadium trioxide (SAZn@DRVO) was developed to expedite the Li^+ desolvation/diffusion kinetics under a low-temperature environment, achieving stable operation even at −50°C. As verified by coupled microscopic imaging, chemical valence- and electronic-state analyses, and electrochemical validation, the optimal SAZn@DRVO-Li electrode delivers long-cycling stability up to 1200 h at −10°C. Even when increasing the plating capacity to 5 mAh cm^{-2}, it retains robust dendrite-free cycling stability for 400 h at 2 mA cm^{-2}. Even down to −50°C, a stable ultralow overpotential below 550 mV is achieved without short circuit. The optimal full cell delivers a high-capacity retention of ~100% after 120 cycles at 0.2C under −20°C, highlighting the feasibility of atom-level catalysis for the development of durable LT-LMBs.

1 | Introduction

The persistent pursuit of high energy density and long duration to satisfy military applications, electric vehicles, and portable electronic devices has intensified extensive research into advanced secondary batteries [1–7]. In spite of graphite anodes in Li-ion batteries, lithium-metal anodes have been identified as promising anodes due to their lowest potential (−3.04 V vs. standard hydrogen electrode) and ultrahigh theoretical capacity of 3860 mAh g^{-1} [8–11]. Unfortunately, lithium-metal batteries (LMBs) have yet to achieve successful commercialization, primarily due to irreversible capacity degradation during long-term

Shikai Yin and Jing Zhang, co-first authors, have contributed equally to this work.

cycling and thermal risks triggered by internal short circuits that originate from uncontrolled lithium dendrite growth [12–16]. Exposed to the harsh environment, low-temperature lithium-metal batteries (LT-LMBs) have attracted widespread interest for applications in subzero environments, such as polar regions of the Earth or outer space [17, 18]. However, when operating below 0°C, LMBs suffer from gradual electrolyte solidification, resulting in the enlarged solvation structure with an increased desolvation barrier and a reduction of capacity [19].

To date, several strategies have been proposed to pursue outstanding low-temperature performance [20–25]. Under the electrolyte engineering, low-freezing-point and low-viscosity solvents have been added to minimize the high freezing point of electrolytes and extend the lithium-ion transport [17, 26, 27]. For example, some functional solvents such as fluoroethylene methyl carbonate (FEMC) weaken the ion–dipole interactions through electron-withdrawing interactions of F atoms, achieving fast desolvation kinetics [21, 28–32]. In addition, emerging functional additives, for example, trimethylsilyl 2,2-difluoro-2-(fluorosulfonyl) acetate (TDFA), are also applied to form an inorganic-rich and thin SEI to reduce interfacial polarization [33]. To prioritize interfacial ion diffusion kinetics while preserving bulk electrolyte conductivity and electrode compatibility, molecular-level pore-sieving interfacial modulation layers on Li metal anodes have been integrated to selectively separate solvation shells and release more free Li^+ for fast transportation [18, 34–36]. Despite the physical pore-sieving capability of porous frameworks (e.g., MOFs or COFs) [37–43], Li^+ ions cannot be effectively sieved due to the enlarged $Li(solvent)_x^+$ clusters with elevated viscosity, which impedes ionic mobility through structural channels. Although some improvements have been achieved, the fundamental mechanism behind the inhibition of dendrite formation remains unclear because the bulk and interfacial ion conductivity of the electrolyte may not be the limiting factors determining the low-temperature performance of LMBs.

As solvated Li^+ ions constitute the primary charge carriers, lithium dendrite growth fundamentally stems from the dissociation of solvated $Li(solvent)_x^+$ and the Li^+/Li^0 diffusion kinetics across the solid electrolyte interphase (SEI) or electrode interface [44–47]. In particular, Li plating dictates sequential interfacial processes of breaking Li^+-solvent interactions, electrochemical reduction to Li atoms, and migration of Li atoms to potential nucleation sites, which consequently influences not only the SEI formation but also the desolvation energy barrier of Li^+ at the electrolyte–electrode interface. Upon decreasing the temperature to −20°C or even lower, dendritic plating behaviors become increasingly problematic, primarily attributed to sluggish interfacial kinetics and the delayed evolution of enlarged $Li(solvent)_x^+$ clusters into free Li^+ by getting rid of solvent shells prior to electrolyte solidification, leading to persistent degradation of low-temperature performance [17, 19, 48, 49]. The electrocatalytic method has already been proposed to decrease the related kinetic barriers in Li and multivalent Zn and Mg batteries [50]. Ideally, increased active-site density can enhance electrocatalytic efficiency to separate solvents in an energy-efficient manner, promoting the dissociation kinetics of $Li(solvent)_x^+$ into free Li^+ for accelerated Li^+ diffusion kinetics. The incorporation of defective sites or single metallic atoms into the modulation layer have been proposed as a feasible way to induce electron orbital delocalization, disrupt the original electronic configuration, and trigger targeted electron redistribution, bringing about enhanced catalytic efficiency [51–53]. Through hybridization of delocalized orbitals between central metal atoms and substrates, active sites with tunable electronic states form structural interfaces that enable improved electron donor/acceptor ability to lower the ion-dipole dissociation energy barrier [54, 55]. Therefore, coupling metallic single atoms into defect sites to maximize the delocalization capability will trigger targeted redistribution of electronic structures to provide more catalytic sites in catalytically accelerating Li^+ desolvation and diffusion.

In this contribution, the interfacial Li^+ solvation shell structure is remodeled for fast desolvation and diffusion kinetics. The strategy of "Single atom-in-defect" as an electron-delocalization catalyst is proposed to enable high-performance LT-LMBs. In this prototype, Zn atoms are anchored onto valence-tunable and defect-rich vanadium trioxide nanoparticles (SAZn@DRVO), upon which the electronic interaction between the solvated Li $(solvent)_x^+$ and these active sites can catalytically weaken and break the Li^+-solvent binding to lower the desolvation energy barriers even under low temperatures. Thereby, the solvation shells are remodeled to facilitate Li^+ desolvation and diffusion kinetics in a more energy-saving manner. In this regard, a large number of free Li^+ ions are released from $Li(solvent)_x^+$ clusters accelerated by electrocatalytic sites, eliminating the uneven Li^+ flux on the Li anode surface to guide the uniform plating of Li near the inner Helmholtz plane (IHP) layer within the electrical double layer (EDL), even under low temperatures, as disclosed in Figure 1A,B. Consequently, SAZn@DRVO-decorated Li electrodes (SAZn@DRVO-Li) achieve an accelerated Li^+ kinetic process and exhibit long-term stripping/plating life of 1200 h with low overpotentials at 2 mA cm^{-2} under −10°C. When increased to 5 mAh cm^{-2}, the optimal Li electrode maintains reversible stability for 400 h at 2 mA cm^{-2}. Upon further decreasing the temperature to −50°C, a stable overpotential below 550 mV without any short circuit is achieved. Matched with lithium iron phosphate (LFP), the as-prepared Li||LFP full cell achieves a high initial capacity of 115 mAh g^{-1} at −10°C and a high-capacity retention of ~100% even under low-temperature conditions of −20°C, providing a pathway for low-temperature Li anodes that can efficiently support LT-LMBs to deliver 68% of their nominal capacities down to −10°C.

2 | Experimental

2.1 | Synthesis of SAZn@DRVO Nanocomposite

The defect-rich V_2O_{3-x} (DRVO) nanocomposite was synthesized based on a combination of the solvothermal method and successive hydrogen treatment. Specifically, 180 mg of purified multiwalled carbon nanotubes (CNTs, Cnano of China) was dispersed in 75 mL of deionized water via continuous sonication to achieve a uniform dispersion. Then 278.4 mg of ammonium metavanadate (NH_4VO_3, Aladdin Scientific) was dissolved in 100 mL of anhydrous ethanol (SINOPHARM) under sonication, forming a clear yellow solution. The NH_4VO_3 solution was then dripped into the CNT dispersion under mechanical stirring, after which the mixture was transferred to a Teflon-lined

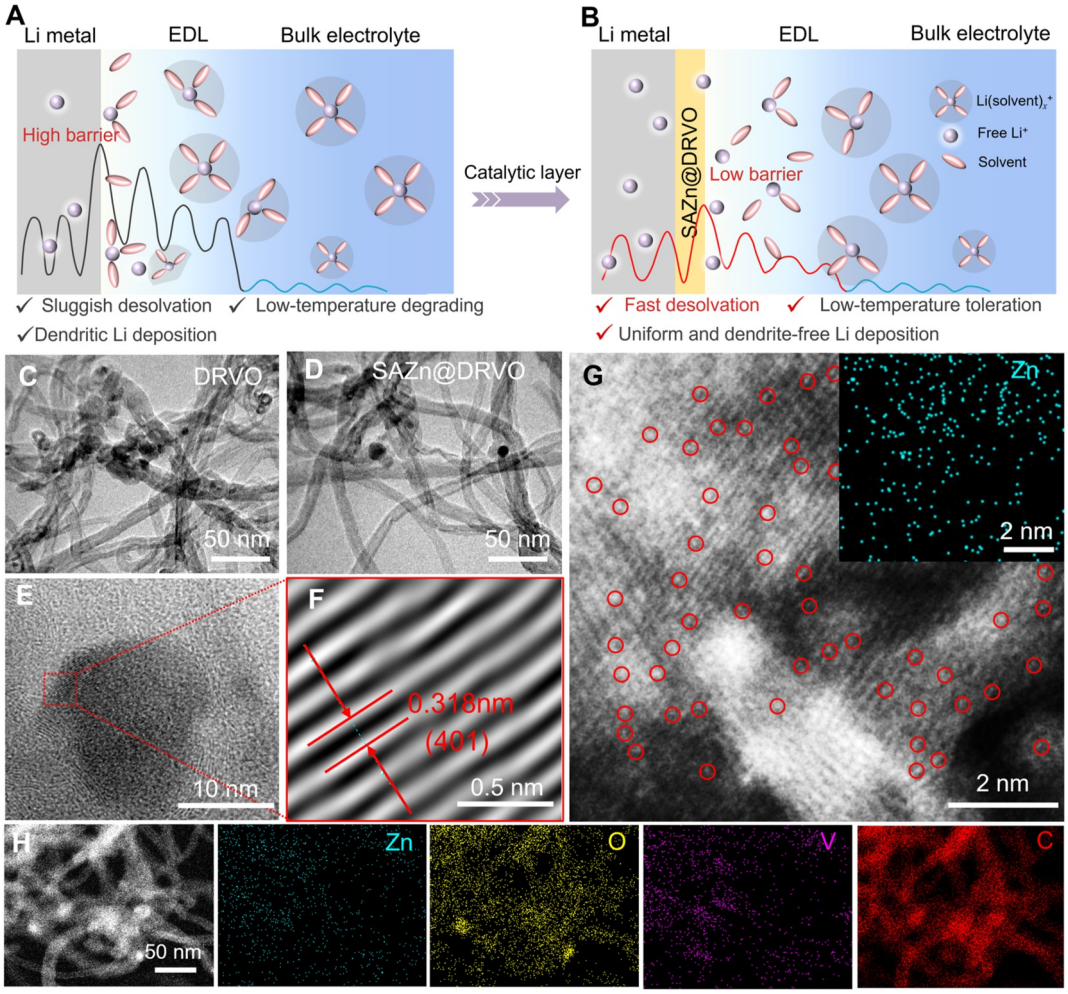

FIGURE 1 | Schematic illustration of the catalytic desolvation effect and atomic morphology characterizations of the SAZn@DRVO nanocomposite. (A, B) Evolution of the electric double layer at the interface of the Li anode induced by the SAZn@DRVO catalyst; TEM images of the (C) DRVO and (D) SAZn@DRVO nanocomposites; (E) HRTEM image of the SAZn@DRVO nanocomposite; (F) IFFT image of the highlighted area of the SAZn@DRVO nanocomposite; (G) HAADF-STEM image of the SAZn@DRVO nanocomposite with an inset showing the corresponding EDX map of elemental Zn distributed in the SAZn@DRVO nanocomposite; (H) EDX elemental maps of the SAZn@DRVO nanocomposite.

stainless-steel autoclave and maintained at 180°C for 24 h. The formed VO_x/CNT solid was collected by filtration and repeatedly washing with deionized water. After freeze-drying, 17 mg of zinc acetate (Aladdin) was added to 20 mL of anhydrous ethanol with 200 mg of VO_x/CNTs, and the mixture was magnetically stirred for 12 h to obtain a uniform suspension. After flash-drying at 80°C, the resultant solid was reduced under the H_2/Ar atmosphere (5 vol% of H_2) at 600°C for 2 h with a heating rate of 5°C min^{-1}, yielding the SAZn@DRVO nanocomposite with uniform atomic Zn-site dispersion. The DRVO nanocomposite was synthesized without atomic precursors.

2.2 | Fabrication of Half and Full Cells

Before assembly, the prepared SAZn@DRVO or DRVO composite (40 mg) with surfactant additives was sonicated in ethanol (80 mL) and further deposited by vacuum filtration onto a commercial separator (Celgard 2350), achieving an areal loading of 0.4 mg cm^{-2} with appropriate thickness. The electrochemical measurements were all conducted using 2025-type coin cells in a glove box filled with a pure Ar atmosphere. During cell assembly, the SAZn@DRVO catalytic layer was oriented toward the working electrodes (lithium and/or copper foils). Then, 40 μL of commercial electrolyte composed of 1 mol L^{-1} lithium bis(trifluoromethyl-sulfonyl)imide (LiTFSI) in a mixed solvent of 1,2-dimethoxyethane (DME) and 1,3-dioxolane (DOL) with a volume ratio of 1:1 was added into the cell.

For fabricating the $LiFePO_4$ (LFP) cathode, a homogeneous slurry was prepared by dispersing commercial LFP powder, conductive carbon black (Super P), and polyvinylidene fluoride (PVDF) binder in N-methyl pyrrolidone (NMP) solvent at a mass ratio of 8:1:1. The electrode was punched into discs of 12 mm in diameter with an average loading of ~2 mg cm^{-2}. The as-designed integrated full cells were assembled with an LFP cathode and a modified SAZn@DRVO-Li anode separated by a Celgard 2350 commercial separator. The electrolyte (1 M LiTFSI with 1 wt% $LiNO_3$ dissolved in a mixed solvent of DME/DOL with a volume ratio of 1:1) at 15 μL mg^{-1} was injected into each coin cell during assembly.

2.3 | Materials Characterizations

The morphologies of the synthesized samples with/without SAZn were characterized using a German Merlin Compact scanning electron microscope (Zeiss) and a JEM-3010 transmission electron microscope. The presence of atomic-scale zinc was verified using a spherical aberration-corrected scanning transmission electron microscope (JEM-ARM200CF NEOARM) coupled with an energy-dispersive spectrometer. X-ray diffraction (XRD) patterns for structural characterization were acquired on an XRD-7000S X-ray diffractometer with Cu Kα radiation by scanning a 2θ range from 10° to 90°. X-ray photoelectron spectra (XPS) were acquired using a Kratos AXIS Ultra DLD spectrometer (Shimadzu Group). Nitrogen adsorption-desorption isotherms were measured on a Micromeritics ASAP 2020 system. Raman spectroscopy was performed on a HORIBA Raman spectrometer (EUROVECTOR EA3000) with a wavelength of 532 nm. Zn *K*-edge XAS measurements were carried out at the ROCK beamline of the French Synchrotron SOLEIL facility. The signal was collected in transmission/fluorescence mode and averaged over 230 scans. A Zn-metal foil was measured simultaneously as a reference for energy calibration. XAS data were further analyzed using Fastosh and Larch software. The calibrated and normalized XANES spectra of SAZn, a Zn-metal foil, and ZnO were compared. EXAFS spectra were extracted using the AUTOBK algorithm. The $\chi(k)$ spectra were isolated by subtracting a smooth polynomial approximating the $\mu_0(E)$ background with $R_{bkg} = 1$ in the data range $k = 0$–13 Å^{-1} of SAZn. The k^2-weighted $\chi(k)$ data were Fourier transformed over 3–10 Å^{-1} after applying a Hanning window function ($dk = 2$ Å^{-1}). Galvanostatic measurements of cells were performed on a battery test system (BTS-5V 10 mA) at various current densities. Electrochemical impedance spectroscopy (EIS) was conducted on a BioLogic workstation (VMP-3) over a frequency range from 100 kHz to 10 mHz. For ex situ scanning electron microscope (ex situ SEM) characterization, Li electrodes were disassembled from coin cells within an argon-filled glove box and then were rinsed with dimethyl ether to remove residual electrolytes and dried in a vacuum overnight at ambient temperature prior to imaging.

3 | Results and Discussion

3.1 | Atomic Morphology Characterization on SAZn@DRVO Nanocomposite

SAZn@DRVO was synthesized using a hydrothermal process followed by thermal reduction. Despite the atomic Zn loading, it still maintains a nanosized porous morphology, which is consistent with DRVO (Supporting Information S1: Figure S1). The SAZn@DRVO nanocomposite exhibits a porous architecture, indicative of effective dispersion of particles and distribution of single atomic Zn during the thermal reduction process. As depicted in the X-ray diffraction (XRD) pattern (Supporting Information S1: Figure S2), the main characteristic diffraction peaks for both nanocomposites are observed at 28.01°, 37.21°, and 55.61°, corresponding to the (401), (303), and (205) lattice planes of the V_2O_3 phase (JCPDS 39-0774), respectively. The inductively coupled plasma emission spectrometry (ICP-OES) shows that the actual loading of Zn in SAZn@DRVO is 3.2 wt%, close to the nominal value (Supporting Information S1: Table S1). Transmission electron microscopy (TEM) analyses in Figure 1C,D confirm that DRVO exhibits a uniform particle size of ~20 nm distributed on porous carbon frameworks affording a surface area of around 125 m^2 g^{-1} to form a physical sieving structure, which is affirmed by the mesopores ranging from 2–5 to 20–50 nm for sieving Li(solvent)$_x^+$ groups with different sizes to get rid of 1,2-dimethoxyethane (DME) or 1,3-dioxolane (DOL) and release more free Li^+ (Supporting Information S1: Figure S3). Combined with the high-resolution TEM (HRTEM) analyses in Figure 1E,F, a lattice spacing of 0.318 nm assigned to the (401) crystal plane of V_2O_3 is further identified. As confirmed by aberration-corrected high-angle annular dark-field scanning transmission electron microscopy (HAADF-STEM) analysis in Figure 1G, the isolated atomic Zn species are uniformly dispersed within the DRVO matrix. Complementary energy-dispersive X-ray spectroscopy (EDX) elemental mapping (Figure 1H) further validates the homogeneous spatial distribution of elemental Zn, O, and V, corroborating no aggregation of V_2O_{3-x} and Zn species at the nanoscale.

3.2 | Electron Delocalization of "SAC-in Defect" in SAZn@DRVO Nanocomposite

To probe the valence state and coordination environment of the atomic sites within the defect-rich catalyst, X-ray absorption spectroscopy (XAS) studies were conducted, leveraging its nearest-neighbor bonding configurations. The X-ray absorption near-edge structure (XANES) spectra (Figure 2A) indicate that the valence state of Zn lies between Zn^0 (Zn foil) and Zn^{2+} (ZnO), but is markedly closer to Zn^{2+}. The chemical surroundings of atomic Zn in SAZn@DRVO were further reflected in the Fourier transform curves of the extended X-ray absorption fine structure (EXAFS), as shown in Figure 2B,C. Two distinct peaks are located at approximately 1.50 and 3 Å in the EXAFS spectra, which collectively suggest the well-dispersed atomic Zn distribution as Zn–O–V coordination within the nanocomposites with no detectable Zn–Zn or Zn–O bonding configurations (Figure 2C). Then, X-ray photoelectron spectroscopy (XPS) was employed to investigate valence-state transitions induced by electronic reconfiguration in the SAZn@DRVO nanocomposite after atomic Zn incorporation (Figure 2D–G and Supporting Information S1: Figure S4). The high-resolution Zn 2p spectrum of SAZn@DRVO (Figure 2D) exhibits exclusively Zn^{2+} signatures at 1021.7 (Zn $2p_{3/2}$) and 1044.7 eV (Zn $2p_{1/2}$). The absence of metallic Zn confirms atomic-scale stabilization via "atom-in-defect" interactions, which is consistent with aberration-corrected HAADF-STEM analysis. For the high-resolution O 1s spectra (Figure 2E), both DRVO and SAZn@DRVO exhibit evolved lattice oxygen (530.2 eV) and defect oxygen (532.5 eV) species [45], accompanied by the shift from V^{2+} (516.4 and 523.7 eV) to V^{3+} (517.6 and 525.1 eV) within the high-resolution V 2p spectra (Figure 2F) [56]. In detail, the ratio of defect oxygen (O_D) decreases from 41% in DRVO to 36% in SAZn@DRVO. At the same time, both the V^{2+} $2p_{3/2}$ and V^{2+} $2p_{1/2}$ species with position shifts decline to 25% and 40%, respectively (Figure 2E, F). This means that Zn atoms are anchored via oxygen-vacancy interactions accompanied by electron transformation, transferring V^{2+} to V^{3+} through vanadium valence reorganization, as demonstrated by the evolution of O_D and V^{2+} species in Figure 2G. Such reconstruction of the electronic structure within the SAZn@DRVO material may facilitate the

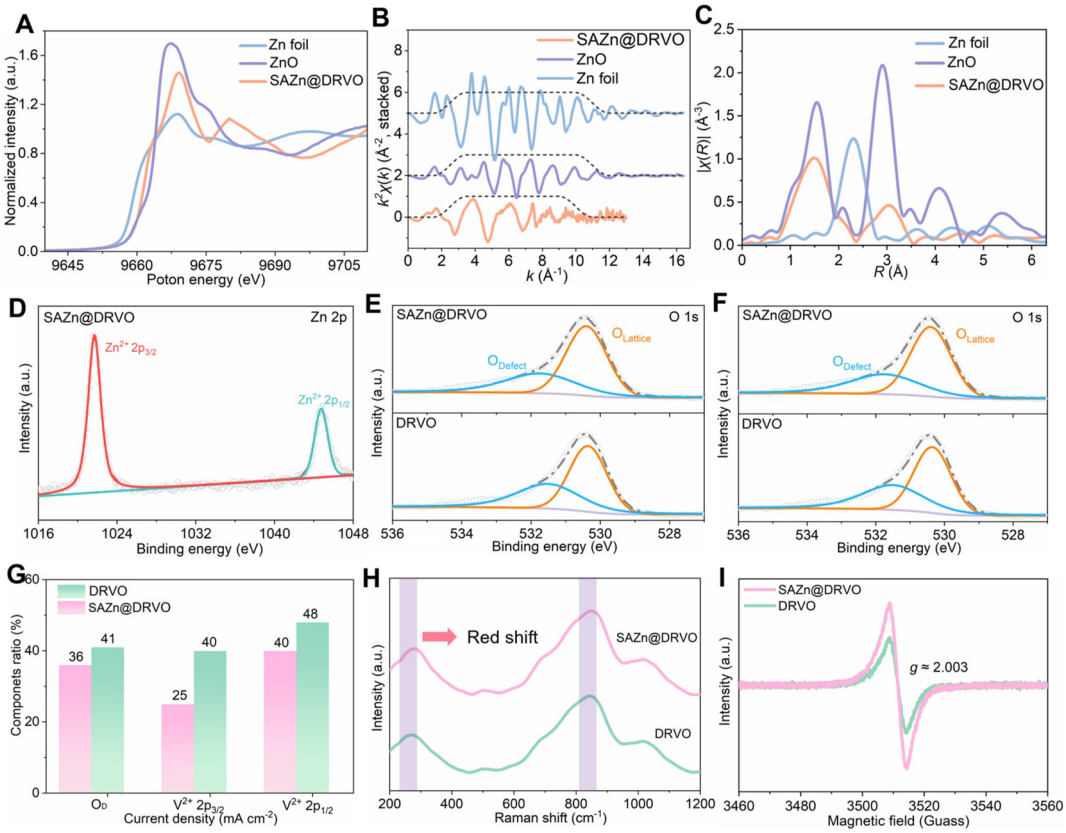

FIGURE 2 | Characterizations of atom-in-defect modulation of electronic reconstruction in the SAZn@DRVO nanocomposite. (A) Normalized Zn K-edge XANES spectra of SAZn@DRVO in comparison with metallic Zn and ZnO; (B) k^2-weighted $\chi(k)$ EXAFS spectra of Zn–O–V, Zn–Zn, and Zn–O bonds and (C) corresponding magnitudes of the Fourier-transformed EXAFS spectra in R-space for the Zn K-edge; high-resolution XPS spectra of (D) Zn 2p, (E) O 1s, and (F) V 2p of the SAZn@DRVO and DRVO nanocomposites; (G) comparison of the variation in the component ratios of O_D, V^{2+} $2p_{3/2}$, and V^{2+} $2p_{1/2}$ species between the SAZn@DRVO and DRVO nanocomposites; (H) comparison of Raman scattering peaks between the SAZn@DRVO and DRVO nanocomposites; (I) EPR spectra of the as-synthesized SAZn@DRVO and DRVO nanocomposites.

generation of more unsaturated sites, ultimately enhancing catalytic activity. In the Raman spectra of SAZn@DRVO and DRVO, characteristic V–O bond vibrational peaks are observed at 273.8, 845.8, and 1017.3 cm^{-1} (Figure 2H) [57]. Upon Zn atom implantation, these peaks exhibit a distinct red shift, attributed to the synergistic effect of atom–defect interactions that modulate the electronic structures. In addition, the I_D/I_G value changed mildly from 1.19 for ODVO to 1.23 for SAZn@DRVO (Supporting Information S1: Figure S5), implying the changed electronic state of the carbon material along with the atom–defect interactions [56]. Furthermore, SAZn@DRVO in the electron paramagnetic resonance (EPR) spectra shown in Figure 2I and Supporting Information S1: Figure S6 exhibits a significantly enhanced signal at $g \approx 2.003$ compared to DRVO. This g-value lies between the characteristic signatures of vanadium-related defects ($g \approx 2.0$–2.1) and oxygen vacancies ($g \approx 1.98$–2.00) [54, 58], confirming the formation of V^{3+} species due to atom–defect interactions in SAZn@DRVO. Such interactions induce strong electron delocalization, which increases the density of unpaired electrons, as evidenced by the amplified EPR response. The anchoring of Zn atoms at oxygen vacancies facilitates electron transformation, oxidizing V^{2+} to V^{3+} (d^3 configuration) and thereby elevating the concentration of paramagnetic centers.

3.3 | Dendrite-Free Performance of Optimal SAZn@DRVO-Li Anodes

To assess the reversibility of the SAZn@DRVO-Li electrode, symmetric cells were assessed. Initially, the electron/ion transport kinetics were evaluated by electrochemical impedance spectroscopy (EIS) in Figure 3A,B. The SAZn@DRVO-Li electrode exhibits markedly reduced charge transfer resistance (135 vs. 185 vs. 265 Ω) with an accelerated ion diffusion slope (12 vs. 18 vs. 24) compared with DRVO-Li and pristine Li. Subsequently, under a current density of 1 mA cm^{-2} with a deposition capacity of 1 mAh cm^{-2}, the SAZn@DRVO-Li electrode displays a stable plating/stripping duration of 900 h with consistently low and stable overpotentials of 160 mV (Figure 3C), distinctly outperforming the DRVO-Li (650 h) and pristine Li electrode (merely 180 h) with fluctuating overpotentials. Additionally, the catalyzed electrode with a Zn loading of 3 wt% delivers the lowest nucleation overpotential (32 vs. 65 vs. 74 vs. 110 mV) and the best cycling stability compared with those containing 1, 2 and 4 wt% Zn (Supporting Information S1: Figure S7), which is thereby selected and valued in this manuscript due to the most optimized desolvation capability. Operating at 2 mA cm^{-2}, the SAZn@DRVO-Li electrode maintains low overpotentials of approximately 200 mV and achieves a cycling lifespan of 1500 h (Figure 3D). Even under a high plating capacity of 5 mAh cm^{-2},

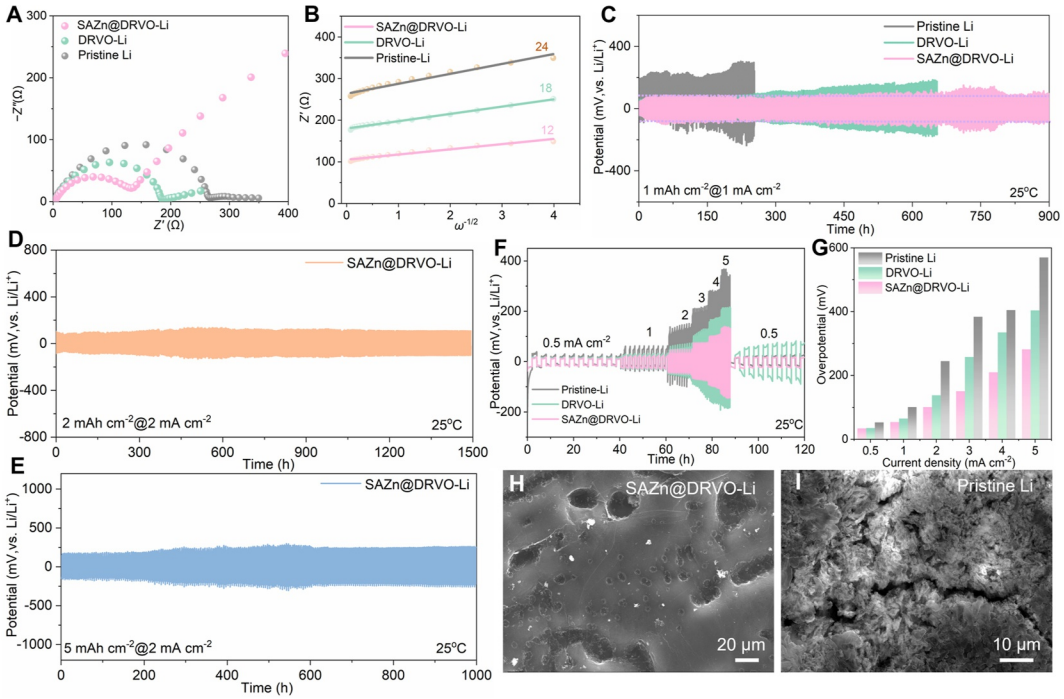

FIGURE 3 | Room-temperature Li electroplating behavior with the SAZn@DRVO catalyst. (A) Comparison of EIS among SAZn@DRVO-Li, DRVO-Li, and pristine Li electrodes and (B) corresponding linear relationship between the real part of the impedance (Z') and the reciprocal exponential ($-1/2$) of the lower angular frequency (ω); galvanostatic plating/stripping stability of the three electrodes under 25°C at different current rates of (C) 1 mA cm^{-2} with 1 mAh cm^{-2}, (D) 2 mA cm^{-2} with 2 mAh cm^{-2}, and (E) 2 mA cm^{-2} with 5 mAh cm^{-2}; (F) comparison of plating/stripping stability at varying current densities and (G) the corresponding voltage gaps of SAZn@DRVO-Li, DRVO-Li, and pristine Li electrodes; (H, I) SEM images of SAZn@DRVO-Li and pristine Li disassembled from the symmetric cells at the end of cycling.

the SAZn@DRVO-Li electrode sustains overpotentials below 450 mV for over 1000 h at 2 mA cm^{-2} (Figure 3E). These enhancements directly demonstrate the exceptional capability of the catalytic SAZn@DRVO layer in modulating lithium ion/atom diffusion kinetics to suppress Li dendrite growth, depending on accelerated Li^+ desolvation and diffusion across the interface. Under a stepwise current-density increase from 0.5 to 5 mA cm^{-2}, the SAZn@DRVO-Li electrode exhibits significantly lower overpotentials than the pristine Li electrode, demonstrating superior interfacial stability, as shown in Figure 3F,G. Notably, even at 5 mA cm^{-2}, it still outputs an ultralow overpotential of merely ~280 mV with excellent stability, whereas the control electrode suffers from severe polarization up to ~570 mV (Figure 3F,G), which is twofold higher than that of the optimal electrode. Subsequently, the postcycling morphological evolution of lithium anodes was assessed by SEM, as shown in Figure 3H,I and Supporting Information S1: Figure S8. The SEM observation reveals a uniform and dendrite-free morphology on the lithium surface of the SAZn@DRVO-Li electrode (Figure 3H). Such smooth deposition behavior is intrinsically attributed to the accelerated desolvation kinetics at the electrode/electrolyte interface, and the generated metal atoms can penetrate the catalytic layer to reach the bottom Li metal for lateral deposition. In contrast, the pristine Li surface after cycling exhibits pronounced cracks with gully-like features (Figure 3I), concurrent with needle-like dendrites on the surface. These needle tips function as localized charge concentrators, inducing cusp effects that promote Li^+ deposition parallel to the needle axis. Such a self-amplifying process accelerates dendritic propagation through continuous tip-directed Li deposition. On the other hand, root fracture of brittle Li dendrites generates electrochemically isolated dead lithium, which critically accelerates electrode pulverization and irreversible volume expansion, directly triggering voltage decay and ultimately inducing battery failure during long-term cycling [45].

To evaluate the environmental viability of SAZn@DRVO-Li electrodes, systematic assessment of batteries at subzero temperatures from 0 to −50°C was conducted. Initially, the Coulombic efficiency (CE) of the SAZn@DRVO-Cu||Li cell was evaluated to be as high as 99% even under a low temperature of −10°C (Figure 4A), whereas the DRVO-Cu||Li and pristine Cu||Li cells only achieve CE values of 97% and 92%, respectively. This divergence highlights the critical role of catalytic SAZn@DRVO in Li^+ desolvation and diffusion to mitigate low-temperature Li^+ deposition losses. Moreover, the Li^+ desolvation and diffusion kinetics are also reflected in the nucleation barrier. Remarkably, SAZn@DRVO-Li electrodes demonstrate significantly reduced nucleation barriers at both −10°C and −20°C compared with pristine Li metal (Figure 4B). For example, under −10°C, the SAZn@DRVO-decorated electrode achieves an ultralow initial nucleation barrier of 80 mV, which is dramatically reduced by 61.2% compared to 206 mV of pristine Li, indicating enhanced ion transport kinetics under low temperature. During the subsequent cycling process, the SAZn@DRVO-Li electrode achieves an ultrastable Li stripping/plating lifespan of up to 1000 h with a minimal overpotential of 180 mV (Figure 4C,D), whereas the pristine Li anode fails within 400 h due to dramatic potential fluctuation (580 mV). Upon decreasing to the harsher condition of −20°C, the SAZn@DRVO-Li electrode still retains much lower

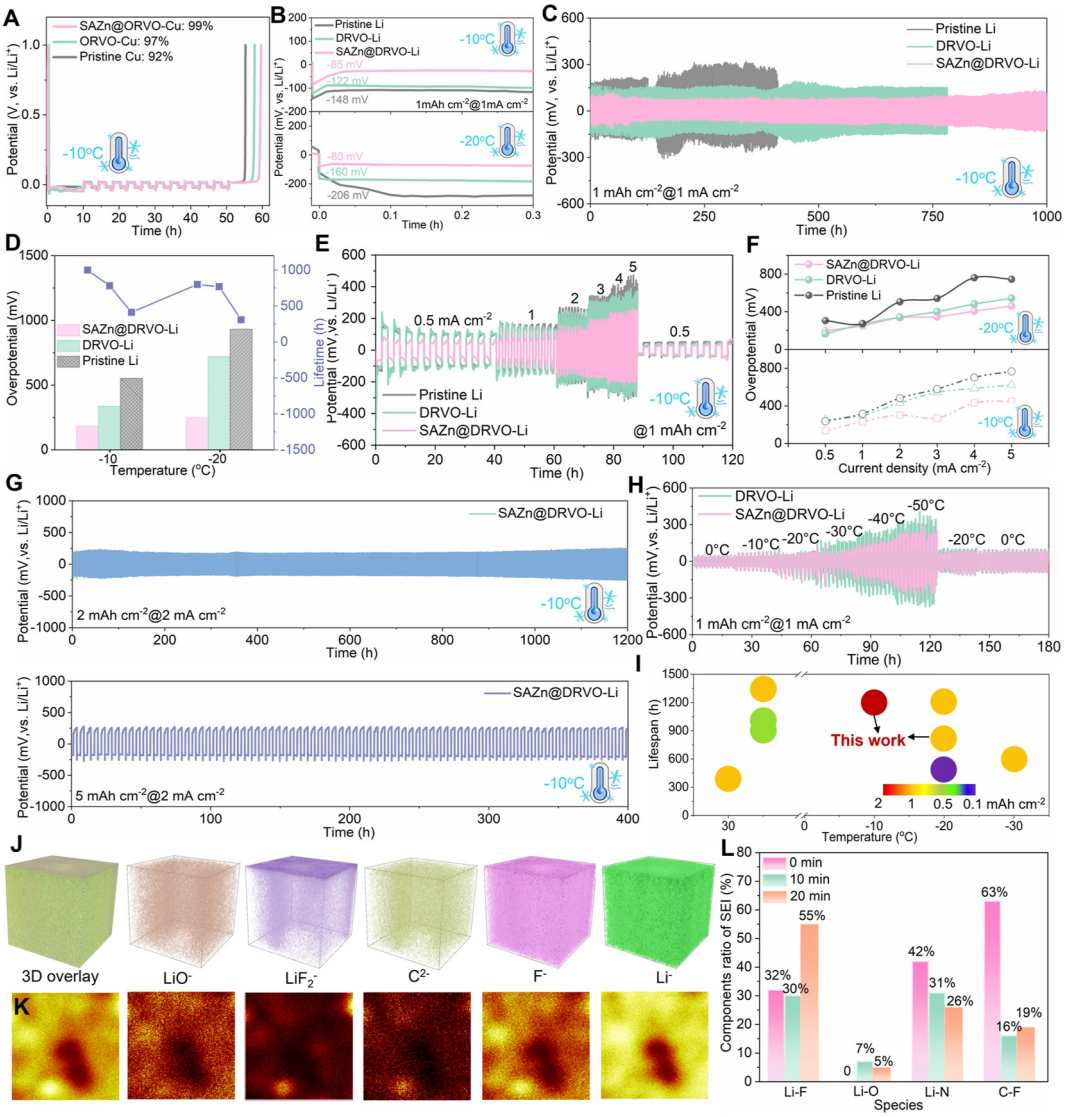

FIGURE 4 | Low-temperature dendrite-free Li plating performance with the SAZn@DRVO catalyst. (A) Aurbach Coulombic efficiency (ACE) tests of different asymmetric Cu||Li cells under −10°C; (B) comparison of initial Li nucleation potentials on different Li electrodes under −10°C and −20°C at 1 mA cm^{-2} with 1 mAh cm^{-2}; (C) galvanostatic plating/stripping stability of the three electrodes under −20°C; (D) overpotentials and cycling lifespan of the SAZn@DRVO-Li, DRVO-Li, and pristine Li electrodes under −10°C and −20°C; (E) plating/stripping stability at varying current densities of the three electrodes under −10°C; (F) comparison of overpotentials of the SAZn@DRVO-Li, DRVO-Li, and pristine Li electrodes at different current densities under −10°C and −20°C; (G) plating/stripping stability of the three electrodes under −10°C at different deposition capacities of 2 and 5 mAh cm^{-2} at 2 mA cm^{-2}; (H) galvanostatic plating/stripping stability of the three electrodes from 0°C to −50°C at 1 mA cm^{-2} with 1 mAh cm^{-2}; (I) comparison of the cycling lifespan of this work at low temperatures with reported literature [23, 59–66]; (J, K) interfacial 3D and 2D reconstruction of organic/inorganic species within the interfacial SEI on the SAZn@DRVO-catalyzed Li electrode after cycling for 20 cycles at −20°C; (L) comparison of the component ratios in the SEI layer on the SAZn@DRVO-Li electrode upon XPS depth profiling.

overpotentials (240 vs. 930 mV) and a stable lifespan of 800 h under 1 mA cm^{-2} (Figure 4D and Supporting Information S1: Figure S9), exhibiting high commercial viability. Upon varying the current density across 0.2–5 mA cm^{-2}, the SAZn@DRVO-Li symmetric cell displays exceptional current tolerance up to 5 mA cm^{-2} compared to the pristine Li electrode (Figure 4E,F and Supporting Information S1: Figure S10), even under an ultralow temperature of −20°C. With an elevated current density of 2 mA cm^{-2} (Figure 4G), the SAZn@DRVO-Li electrode under −10°C maintains low overpotentials and exceptional cycling stability up to 1200 h. Even under an extremely high areal capacity of 5 mAh cm^{-2}, the SAZn@DRVO-modified Li electrode still delivers a quite lower overpotential of ~500 mV and ultrastable operation for 400 h (Figure 4G), further confirming its viability for high-rate and low-temperature applications. More remarkably, even across the extreme low-temperature gradient from 0°C to −50°C, the modified Li electrode delivers ultrastrong temperature robustness, with the steadily increasing overpotential remaining below 550 mV without any phenomenon of dendrite growth due to the enhanced Li^+ desolvation catalyzed by SAZn@DRVO (Figure 4H), demonstrating highly reversible lithium plating/stripping compared to other reported LMBs (Figure 4I and Supporting Information S1: Table S2) [23, 59–66]. Owing to the robustness of SAZn@DRVO, a well-distributed Li

with a smooth and uniform SEI layer (such as LiF_2^-, LiO^-, and C^{2-} species) is observed for the cycled SAZn@DRVO-Li electrode under a low temperature of −20°C, as demonstrated by the 3D morphology reconstruction using time-of-flight secondary-ion mass spectrometry (TOF-SIMS) in Figure 4J,K and Supporting Information S1: Figure S11. Furthermore, the SEI film uniformity of Li plating was detected by depth-profile XPS analysis. As presented in the high-resolution Li 1s spectra in Supporting Information S1: Figure S12, a prominent Li–F peak is located around 55.2 eV, and the F 1s spectra (Supporting Information S1: Figure S12A,B) reveal a strong Li–F peak close to 686.5 eV at the same time, attributed to the decomposition of LiTFSI on the Li metal surface. As the etching proceeds from 0 to 20 min, a marked increase in Li–F species content (from 32% to 55%) coincides with a decline in the C–F peak (690.2 eV) from 63% to 19%, originating from the LiTFSI (Figure 4L and Supporting Information S1: Figure S12B), which collectively confirms the formation of a Li–F-enriched SEI on the SAZn@DRVO-regulated Li surface. Meanwhile, the N 1s spectrum shows a reduction in Li–N species content from 42% to 26% over the etching period, which indicates the incorporation of Li_3N into the SEI layer (Supporting Information S1: Figure S12C). Overall, a uniformly formed and distributed mixture of organic and inorganic components in the SEI is demonstrated by combining TOF-SIMS with depth-profile XPS analyses.

3.4 | Robust Temperature Electrochemical Performance of Full Cells

The practical application potential of SAZn@DRVO is further validated in full cells. Initially, the EIS curves (Figure 5A) disclose a significantly lower R_{ct} of 15 Ω for the SAZn@DRVO-Li||LFP cell compared to 105 Ω for the DRVO-Li||LFP and 180 Ω for pristine Li||LFP full cells. At the same time, the distinct reduction in the linear slope (179 vs. 344 vs. 364) of the Warburg impedance signifies faster charge and ion transfer kinetics (Figure 5B). Cyclic voltammetry (CV) analyses in Figure 5C and Supporting Information S1: Figure S13 show a single pair of redox peaks centered at 3.2 V (cathodic) and 3.6 V (anodic), assigned to the reversible redox reactions during Li^+ intercalation/deintercalation [67], respectively. Meanwhile, the SAZn@DRVO-Li||LFP cell exhibits closer redox peak separation (ΔE = 0.24 vs. 0.30 vs. 0.44 V) alongside amplified current peak intensity, which denotes smaller polarization and faster reaction kinetics resulting from accelerated interfacial Li^+ desolvation and diffusion kinetics catalyzed by the SAZn@DRVO layer (Figure 5C). During the following cycles, the SAZn@DRVO-Li||LFP cell maintains excellent overlap with good symmetry (Supporting Information S1: Figure S13), which indicates enhanced reversibility of the redox reaction. Subsequently, the cycling performances of the full cell at 1C were evaluated (1C = 170 mA g^{-1}), as shown in Figure 5D. Notably, the

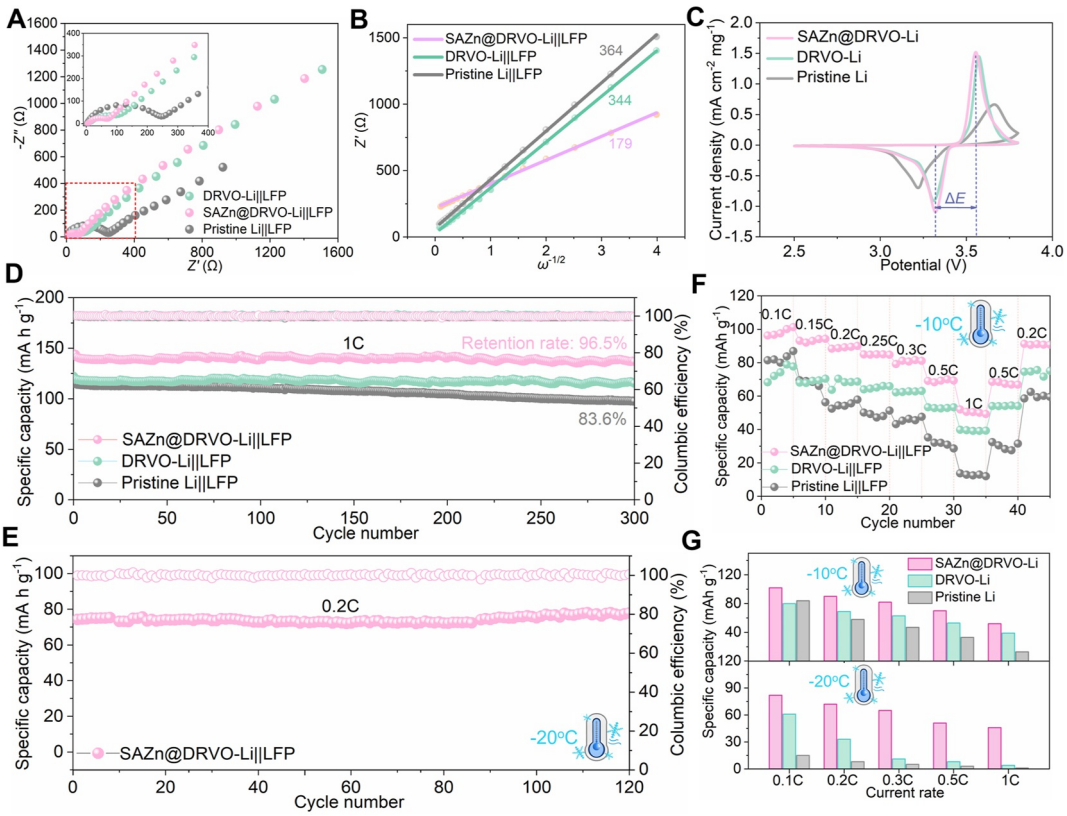

FIGURE 5 | Low-temperature electrochemical performance of full batteries based on the SAZn@DRVO-Li anode. (A) EIS profiles carried out on SAZn@DRVO-Li||LFP, SDRVO-Li||LFP, and pristine Li||LFP full cells and (B) corresponding linear relationship between the real part of the impedance (Z') and the reciprocal exponential (−1/2) of the lower angular frequency (ω); (C) comparison of CV curves of SAZn@DRVO-Li||LFP, DRVO-Li||LFP, and pristine Li||LFP full cells at 0.1 mV s^{-1}; (D) cycling performance of the different paired full cells at 1C at room temperature; (E) cycling performance of the paired full cell at 0.2C under −20°C; (F) rate performance of the three paired full cells under −10°C; (G) capacity comparison of the three paired full cells at different current rates under −10°C and −20°C, respectively.

SAZn@DRVO-Li||LFP full cell delivers a high initial capacity of 145 mAh g^{-1} and sustains exceptional stability with a capacity retention of 96.5% after 300 cycles, much higher than 115 mAh g^{-1} with a retention of merely 83.6% for the pristine Li||LFP cell (Figure 5D). Upon varying the current rate from 0.1C to 6C, the SAZn@DRVO-Li||LFP cell delivers superior rate performance, achieving a high discharge capacity of 77 mAh g^{-1} with small polarization at a high rate of 6C (Supporting Information S1: Figures S14 and S15). Upon decreasing the temperature to −10°C, the SAZn@DRVO-Li||LFP full cell displays a high initial capacity of 115 mAh g^{-1} and retains nearly 100% capacity after 75 cycles at 0.1C, whereas the pristine Li||LFP cell shows an inferior initial capacity of 84 mAh g^{-1} (Supporting Information S1: Figure S16). Although the LFP loading is boosted to as high as around 10 mg cm^{-2}, the full cell still delivers a high specific capacity of 144 mAh g^{-1} under a low temperature of 0°C at 0.1C and a high-capacity retention ratio of ~100% after 80 cycles (Supporting Information S1: Figure S17). Even under −20°C, it remains stable at a specific capacity of 74 mAh g^{-1} with nearly 100% capacity retention after 120 cycles (Figure 5E). Thereafter, the SAZn@DRVO-Li||LFP full cell provides an ultrasteady rate capacity under varying current rates at both −10°C and −20°C. The SAZn@DRVO-Li||LFP cell delivers the discharge capacities of 102, 90, 81, 70, and 52 mAh g^{-1} with stable discharge plateaus under −10°C at varying current rates of 0.1, 0.2, 0.3, 0.5, and 1C (Figure 5F,G and Supporting Information S1: Figure S18), respectively, which are much higher than those of the pristine Li||LFP cell under the same conditions. Moreover, it exhibits a gradual capacity decrease with increasing current rates even under −20°C (Supporting Information S1: Figure S19), contrasting sharply with the pristine Li||LFP cell, which undergoes sudden failure and complete capacity loss from 0.2C, demonstrating the expedited kinetics due to the uniform Li^+ flux accelerated by SAZn@DRVO.

4 | Conclusions

In summary, the strategy of electron-delocalization catalysis of "Single atom-in-Defect" is proposed to realize high-performance lithium-metal batteries with enhanced low-temperature resilience enabled by anchoring single-atomic Zn into defect-rich vanadium trioxide (SAZn@DRVO). As evidenced by coupled microscopic imaging, chemical valence- and electronic-state analyses, and electrochemical measurements, the energy barriers of desolvation and diffusion are reduced for facilitating Li^+ kinetics toward effective dendrite suppression. Under a low temperature of −10°C, the as-fabricated SAZn@DRVO-Li stabilizes for 1200 h with minimal overpotentials. Even under a high current density with a high deposition capacity (5 mAh cm^{-2}, 2 mA cm^{-2}), a lifespan of 400 h is achieved, demonstrating robust capability in dendrite suppression. At extremely low temperatures down to −50°C, a stable ultralow overpotential below 550 mV is achieved without short circuit. The paired SAZn@DRVO-Li||LFP full cell delivers a high-capacity retention of ~100% after 120 cycles at 0.2C even under −20°C, demonstrating the potential application of functional catalysts for stable LT-LMBs.

Author Contributions

Shikai Yin: data curation, investigation. **Jing Zhang:** conceptualization, data curation, project administration, writing – original draft. **Mannan Yang:** formal analysis, investigation, resources. **Yang Hu:** formal analysis, investigation. **Bixian Chen:** data curation, investigation. **Na Tian:** funding acquisition, supervision. **Hao Li:** visualization. **Caiyin You:** visualization. **Dongmao Jiao:** resources. **Zhenjiang Cao:** investigation. **Yongzheng Zhang:** investigation, methodology. **Lin Li:** investigation. **Dong Wang:** investigation, methodology. **Honzhen Lin:** funding acquisition, methodology. **Jian Wang:** conceptualization, methodology, project administration, supervision, visualization, writing – review and editing.

Acknowledgments

This study was financially supported by the National Natural Science Foundation of China (Grant Nos. 22309144, 52171191, 52371198, and 22572217), the National Key R&D Program of China (Grant No. 2021YFA1201503), the Scientific Research Program of Shaanxi Provincial Education Department (Grant No. 25JP119), the Natural Science Foundation of Jiangsu Province (Grant Nos. BK 20210130 and BK J20251840), the Open Project of Inner Mongolia Engineering Research Center of Lithium-Sulfur Battery Energy Storage (Grant No. MDK2025071), and the opening funding from the Key Laboratory of Engineering Dielectrics and Its Application (Grant No. KFM202507). Jian Wang and Jing Zhang additionally acknowledge the funding provided by the Alexander von Humboldt Foundation and the Youth Innovation Team of Shaanxi Universities. The authors thank the technical assistance provided by Nano-X, Suzhou Institute of Nano-tech and Nano-bionics, Chinese Academy of Sciences; and the Advanced Material Analysis and Test Center, Xi'an University of Technology. The authors also acknowledge Synchrotron SOLEIL for the provision of beamtime under proposal number 20250051, and they thank Dr. S. Belin for assistance in using the "ROCK" beamline. The beamtime work was supported by a public grant overseen by the French National Research Agency (ANR) as part of the "Investissements d'Avenir" program (reference: ANR-10-EQPX-45). Open Access funding enabled and organized by Projekt DEAL.

Conflicts of Interest

The authors declare no conflicts of interest.

Data Availability Statement

The data that support the findings of this study are available from the corresponding author upon reasonable request.

References

1. Z. Guo, Z. Cui, and A. Manthiram, "Crossover Effects of Transition-Metal Ions on Lithium-Metal Anode in Localized High Concentration Electrolytes," *Advanced Functional Materials* 35, no. 40 (2025): 2501743, https://doi.org/10.1002/adfm.202501743.

2. J. Wang, J. Zhang, S. Duan, et al., "Interfacial Lithium-Nitrogen Bond Catalyzes Sulfide Oxidation Reactions in High-Loading Li_2S Cathode," *Chemical Engineering Journal* 429 (2025): 132352, https://doi.org/10.1016/j.cej.2021.132352.

3. T. Wang, B. Chen, Y. Liu, et al., "Fatigue of Li Metal Anode in Solid-State Batteries," *Science* 388, no. 6744 (2025): 311–316, https://doi.org/10.1126/science.adq6807.

4. J. Zhang, R. He, L. Jia, et al., "Strategies for Realizing Rechargeable High Volumetric Energy Density Conversion-Based Aluminum–Sulfur

Batteries," *Advanced Functional Materials* 33, no. 48 (2023): 2305674, https://doi.org/10.1002/adfm.202305674.

5. J.-J. Sun, Z.-H. Zhang, P. Ma, and H.-B. Li, "Construction of Strong Sb/MXene Interface Toward Fast and High-Capacity Lithium-Ion Storage," *Rare Metals* 44, no. 11 (2025): 8388–8403, https://doi.org/10.1007/s12598-025-03541-2.

6. P. Lei, X. Zhou, X. Wu, H. Fu, H. Li, and H. Huang, "Biomimetic Construction of Oxygen Vacancy-Rich In_2O_3/In_2S_3@C Heterostructures With Built-in Electric Field for Boosting Bidirectional Regulation of Polysulfides in Lithium-Sulfur Batteries," *Chemical Engineering Journal* 516 (2025): 164100, https://doi.org/10.1016/j.cej.2025.164100.

7. H. Luo, X. Su, Z. Chen, et al., "Aqueous Iron-Ions Batteries: Status, Solutions, and Prospects," *Advanced Materials* 37, no. 40 (2025): 2507978, https://doi.org/10.1002/adma.202507978.

8. J. Ding, T. Du, L. R. Jensen, et al., "High-Performance Dendrite-Free Lithium Metal Anode Based on Metal-Organic Framework Glass," *Advanced Materials* 36, no. 29 (2024): 2400652, https://doi.org/10.1002/adma.202400652.

9. Y. Wang, Y. Li, X. Wang, et al., "Shape-Controlled Reversible Li Plating-Stripping for Stable and High-Rate Anode-Free Lithium Metal Batteries," *Advanced Materials* 37, no. 18 (2025): 2420373, https://doi.org/10.1002/adma.202420373.

10. J. Wang, J. Zhang, S. Duan, et al., "Lithium Atom Surface Diffusion and Delocalized Deposition Propelled by Atomic Metal Catalyst Toward Ultrahigh-Capacity Dendrite-Free Lithium Anode," *Nano Letters* 22, no. 19 (2022): 8008–8017, https://doi.org/10.1021/acs.nanolett.2c02611.

11. A. Cheng, P. Gao, R. Wang, K. Wang, and K. Jiang, "Mixed Ion-Electron Conducting Li Ag Alloy Anode Enabling Stable Li Plating/Stripping in Solid-State Batteries via Enhanced Li Diffusion Kinetic," *Green Energy and Intelligent Transportation* 4, no. 1 (2025): 100179, https://doi.org/10.1016/j.geits.2024.100179.

12. J. Wang, H. Hu, J. Zhang, et al., "Hydrophobic Lithium Diffusion-Accelerating Layers Enables Long-Life Moisture-Resistant Metallic Lithium Anodes in Practical Harsh Environments," *Energy storage materials* 52 (2022): 201−219, https://doi.org/10.1016/j.ensm.2022.08.004.

13. Z. Liu, X. Fu, Z. Li, et al., "Integrated Anode With 3D Electron/Ion Conductive Network for Stable Lithium Metal Batteries," *Energy Storage Materials* 66 (2024): 103201, https://doi.org/10.1016/j.ensm.2024.103201.

14. J. Wang, L. Jia, H. Liu, et al., "Multi-Ion Modulated Single-Step Synthesis of a Nanocarbon Embedded With a Defect-Rich Nanoparticle Catalyst for a High Loading Sulfur Cathode," *ACS Applied Materials & Interfaces* 12, no. 11 (2020): 12727−12735, https://doi.org/10.1021/acsami.9b21509.

15. J. Chen, Y. Zhang, H. Lu, et al., "Electrolyte Solvation Chemistry to Construct an Anion-Tuned Interphase for Stable High-Temperature Lithium Metal Batteries," *eScience* 3, no. 4 (2023): 100135, https://doi.org/10.1016/j.esci.2023.100135.

16. J. Wang, L. Li, H. Hu, et al., "Toward Dendrite-Free Metallic Lithium Anodes: From Structural Design to Optimal Electrochemical Diffusion Kinetics," *ACS Nano* 16, no. 11 (2022): 17729–17760, https://doi.org/10.1021/acsnano.2c08480.

17. C. B. Jin, N. Yao, Y. Xiao, et al., "Taming Solvent–Solute Interaction Accelerates Interfacial Kinetics in Low-Temperature Lithium-Metal Batteries," *Advanced Materials* 35, no. 3 (2022): 2208340, https://doi.org/10.1002/adma.202208340.

18. T. Li, A. Wang, J. Liao, et al., "Organic Sulfurization Interface Enabled the Long-Lifespan Lithium Metal Anode for Ah-Class Pouch Cells," *Rare Metals* 44, no. 8 (2025): 5301–5309, https://doi.org/10.1007/s12598-025-03302-1.

19. Z. Li, R. Yu, S. Weng, Q. Zhang, X. Wang, and X. Guo, "Tailoring Polymer Electrolyte Ionic Conductivity for Production of Low- Temperature Operating Quasi-all-Solid-State Lithium Metal Batteries," *Nature Communications* 14, no. 1 (2023): 482, https://doi.org/10.1038/s41467-023-35857-x.

20. M. Fang, X. Yue, Y. Dong, Y. Chen, and Z. Liang, "A Temperature-Dependent Solvating Electrolyte for Wide-Temperature and Fast-Charging Lithium Metal Batteries," *Joule* 8, no. 1 (2024): 91–103, https://doi.org/10.1016/j.joule.2023.12.012.

21. T. Ma, Y. Ni, Q. Wang, et al., "Optimize Lithium Deposition at Low Temperature by Weakly Solvating Power Solvent," *Angewandte Chemie International Edition* 61, no. 39 (2022): e202207927, https://doi.org/10.1002/anie.202207927.

22. J. Wang, J. Zhang, S. Cheng, et al., "Long-Life Dendrite-Free Lithium Metal Electrode Achieved by Constructing a Single Metal Atom Anchored in a Diffusion Modulator Layer," *Nano Letters* 21, no. 7 (2021): 3245–3253, https://doi.org/10.1021/acs.nanolett.1c00534.

23. P. Zhai, Q. He, H. Jiang, et al., "Thickness-Dependence of 2D g-C_3N_4 Artificial Interface Layers on Lithium Metal Deposition," *Advanced Energy Materials* 14, no. 5 (2023): 2302730, https://doi.org/10.1002/aenm.202302730.

24. L. T. Zhou, Q. Q. Zhang, H. D. Yuan, et al., "Multifunctional C/ZnS Nanocapsules Modified Carbon Cloth as 3D Conductive Collector and Lithium Host for Stable Lithium Metal Anodes," *Rare Metals* 44, no. 8 (2025): 5320–5332, https://doi.org/10.1007/s12598-025-03321-y.

25. H. Luo, H. Guo, X. Li, et al., "Aqueous Manganese-Ion Batteries: The Past, Present, and Future," *Matter* 8, no. 12 (2025): 102379, https://doi.org/10.1016/j.matt.2025.102379.

26. J. Jang, C. Wang, G. Kang, et al., "Miniature Li^+ Solvation by Symmetric Molecular Design for Practical and Safe Li-Metal Batteries," *Nature Energy* 10, no. 4 (2025): 502–512, https://doi.org/10.1038/s41560-025-01733-9.

27. C. Hu, S. Guo, F. Huang, et al., "Carbonate Ester-Based Sodium Metal Battery With High-Capacity Retention at −50°C Enabled by Weak Solvents and Electrodeposited Anode," *Angewandte Chemie International Edition* 63, no. 40 (2024): e202407075, https://doi.org/10.1002/anie.202407075.

28. Y. Shuai, Y. Hu, X. Gong, et al., "Fluorine-Free Electrolytes for High-Performance and Low-Cost Lithium Metal Batteries," *Chemical Engineering Journal* 505 (2025): 159101, https://doi.org/10.1016/j.cej.2024.159101.

29. J. Jiang, M. Li, X. Liu, et al., "Multifunctional Additives to Realize Dendrite-Free Lithium Deposition in Carbonate Electrolytes Toward Low-Temperature Li Metal Batteries," *Advanced Energy Materials* 14, no. 27 (2024): 2400365, https://doi.org/10.1002/aenm.202400365.

30. H. Ji, J. Xiang, Y. Li, et al., "Liquid–Liquid Interfacial Tension Stabilized Li-Metal Batteries," *Nature* 643, no. 8074 (2025): 1255–1262, https://doi.org/10.1038/s41586-025-09293-4.

31. X. Liu, X. Zheng, X. Qin, et al., "Temperature-Responsive Solid-Electrolyte-Interphase Enabling Stable Sodium Metal Batteries in a Wide Temperature Range," *Nano Energy* 103 (2022): 107746, https://doi.org/10.1016/j.nanoen.2022.107746.

32. J. Liu, H. Xu, X. B. Li, H. N. Ming, S. L. Shang, and S. Liu, "Lithophilic Alloy and 3D Grid Structure Synergistically Reinforce Dendrite-Free Li–Sn/Cu Anode for Ultra-Long Cycle Life Lithium Metal Battery," *Rare Metals* 44, no. 6 (2025): 3735–3748, https://doi.org/10.1007/s12598-024-03102-z.

33. E. Park, Y.-H. Lee, S.-H. Huh, J. Huh, Y.-E. Sung, and S.-H. Yu, "Bifunctional Trimethylsilyl-Modified Fluorinated Ester Additive for LiF-Rich Solid Electrolyte Interphase in Lithium Metal Batteries," *Energy Storage Materials* 78 (2025): 104271, https://doi.org/10.1016/j.ensm.2025.104271.

34. F. Ding, S. Liu, H. Xu, Z. Li, Z. Yan, and H. Cui, "Vinylidene Carbonate Drived Ultra-Stable Artificial SEI for Lithium Metal Anode With Ultra-Long Life," *Chemical Engineering Journal* 518 (2025): 164411, https://doi.org/10.1016/j.cej.2025.164411.

35. C. Y. Im, G. Y. Lee, J. G. Kim, J. H. Choi, and S. J. Kim, "Controlling Lithium Surface Diffusivity via 2D $PtTe_2$, $PdTe_2$, and $NiTe_2$ Coatings for Anode-Free and Lithium Metal Batteries," *Advanced Materials* 37, no. 33 (2025): 2501261, https://doi.org/10.1002/adma.202501261.

36. X. Su, S. Li, Z. Chen, et al., "Steering $Zn(ClO_4)_2$ Electrolyte: Trifunctional Polycationic Artificial Interphase for Wide-Temperature Ah-Level Zn-I2 Pouch Cells," *Energy Storage Materials* 85 (2026): 104900, https://doi.org/10.1016/j.ensm.2026.104900.

37. Z. Chen, J. Pan, W. Huang, et al., "Heterogeneity-Segment Charge-Induced-Coupling Catalysis of Component-Selective-Type Covalent Organic Frameworks Interface Toward Stabilizing Lithium Metal Anode," *ACS Nano* 19, no. 13 (2025): 13160–13174, https://doi.org/10.1021/acsnano.4c18473.

38. D. Chen, S. Huang, L. Zhong, et al., "In Situ Preparation of Thin and Rigid COF Film on Li Anode as Artificial Solid Electrolyte Interphase Layer Resisting Li Dendrite Puncture," *Advanced Functional Materials* 30, no. 7 (2019): 1907717, https://doi.org/10.1002/adfm.201907717.

39. M. H. Nguyen, J. Shin, M.-R. Kim, Q. V. Nguyen, J. Cha, and S. Park, "Confining Li^+ Solvation in Core–Shell Metal–Organic Frameworks for Stable Lithium Metal Batteries at 100°C," *Nano-Micro Letters* 18, no. 1 (2026): 135, https://doi.org/10.1007/s40820-025-01988-7.

40. L. Li, H. Tu, J. Wang, et al., "Electrocatalytic MOF-Carbon Bridged Network Accelerates Li^+-Solvents Desolvation for High Li^+ Diffusion Toward Rapid Sulfur Redox Kinetics," *Advanced Functional Materials* 33, no. 13 (2023): 2212499, https://doi.org/10.1002/adfm.202212499.

41. X. Zhang, X. Li, Y. Zhang, et al., "Accelerated Li^+ Desolvation for Diffusion Booster Enabling Low-Temperature Sulfur Redox Kinetics via Electrocatalytic Carbon-Grazfted-CoP Porous Nanosheets," *Advanced Functional Materials* 33, no. 36 (2023): 2302624, https://doi.org/10.1002/adfm.202302624.

42. X.-D. Zhou, X.-X. Wu, H.-J. Fu, et al., "Self-Assembled Co-MOF@MXene Heterostructures as Bifunctional Electrocatalysts for High-Performance Lithium-Sulfur Batteries," *Materials Today Energy* 52 (2025): 101950, https://doi.org/10.1016/j.mtener.2025.101950.

43. P. Xue, C. Guo, L. Li, et al., "A MOF-Derivative Decorated Hierarchical Porous Host Enabling Ultrahigh Rates and Superior Long-Term Cycling of Dendrite-Free Zn Metal Anodes," *Advanced Materials* 34, no. 14 (2022): 2110047, https://doi.org/10.1002/adma.202110047.

44. J. Wang, J. Zhang, J. Wu, et al., "Interfacial "Single-Atom-in-Defects" Catalysts Accelerating Li^+ Desolvation Kinetics for Long-Lifespan Lithium-Metal Batteries," *Advanced Materials* 35, no. 39 (2023): 2302828, https://doi.org/10.1002/adma.202302828.

45. J. Zhang, R. He, Q. Zhuang, et al., "Tuning 4f-Center Electron Structure by Schottky Defects for Catalyzing Li Diffusion to Achieve Long-Term Dendrite-Free Lithium Metal Battery," *Advanced Science* 9, no. 23 (2022): 2202244, https://doi.org/10.1002/advs.202202244.

46. A. Hu, F. Li, W. Chen, et al., "Ion Transport Kinetics in Low-Temperature Lithium Metal Batteries," *Advanced Energy Materials* 12, no. 42 (2022): 2202432, https://doi.org/10.1002/aenm.202202432.

47. J. Wang, H. Liu, J. Zhang, et al., "Polysulfide-Mediated Solvation Shell Reorganization for Fast Li^+ Transfer Probed by In-Situ Sum Frequency Generation Spectroscopy," *Energy Storage Mater* 67 (2024): 103289, https://doi.org/10.1016/j.ensm.2024.103289.

48. L. Luo, K. Chen, H. Chen, et al., "Enabling Ultralow-Temperature (−70°C) Lithium-Ion Batteries: Advanced Electrolytes Utilizing Weak-Solvation and Low-Viscosity Nitrile Cosolvent," *Advanced Materials* 36, no. 5 (2023): 2308881, https://doi.org/10.1002/adma.202308881.

49. Y. Chen, Q. He, Y. Zhao, et al., "Breaking Solvation Dominance of Ethylene Carbonate via Molecular Charge Engineering Enables Lower Temperature Battery," *Nature Communications* 14, no. 1 (2023): 8326, https://doi.org/10.1038/s41467-023-43163-9.

50. C. Ye, H. Li, Y. Chen, et al., "The Role of Electrocatalytic Materials for Developing Post-Lithium Metal||Sulfur Batteries," *Nature Communications* 15, no. 1 (2024): 4797, https://doi.org/10.1038/s41467-024-49164-6.

51. J. Wang, J. Zhang, Y. Zhang, et al., "Atom-Level Tandem Catalysis in Lithium Metal Batteries," *Advanced Materials* 36, no. 26 (2024): 2402792, https://doi.org/10.1002/adma.202402792.

52. J. Zhang, L. Pan, L. Jia, et al., "Delocalized Electron Engineering of MXene-Immobilized Atomic Catalysts Toward Fast Desolvation and Dendritic Inhibition for Low-Temperature Zn Metal Batteries," *Nano Letters* 25, no. 10 (2025): 3756–3765, https://doi.org/10.1021/acs.nanolett.4c05503.

53. J. Pu, Z. Wang, P. Xue, K. Zhu, J. Li, and Y. Yao, "The Effect of NiO-Ni_3N Interfaces in In-Situ Formed Heterostructure Ultrafine Nanoparticles on Enhanced Polysulfide Regulation in Lithium-Sulfur Batteries," *Journal of Energy Chemistry* 68 (2022): 762–770, https://doi.org/10.1016/j.jechem.2021.12.043.

54. J. Zhang, F. Liu, R. He, et al., "Taming Interfacial Ion-Dipole Interactions With d-Orbital Delocalized Electron Catalysis Expediates Low-Temperature Li Metal Batteries," *Advanced Materials* 38, no. 4 (2025): e10894, https://doi.org/10.1002/adma.202510894.

55. G. Wu, Y. Fan, J. Li, et al., "Facilitated Polysulfide Redox Conversion by Delocalized Electrons in MBene Heterointerface for Highly Stable Lithium–Sulfur Batteries," *Nano-Micro Letters* 18, no. 1 (2026): 252, https://doi.org/10.1007/s40820-026-02100-3.

56. J. Zhang, L. Li, M. Yang, et al., "Electron-Delocalization Catalyzers for High Performance, Low-Temperature Li–S Batteries," *Chemical Communications* 60, no. 94 (2024): 13891–13894, https://doi.org/10.1039/d4cc04372c.

57. G. P. Pandey, T. Liu, E. Brown, et al., "Mesoporous Hybrids of Reduced Graphene Oxide and Vanadium Pentoxide for Enhanced Performance in Lithium-Ion Batteries and Electrochemical Capacitors," *ACS Applied Materials and Interfaces* 8, no. 14 (2016): 9200–9210, https://doi.org/10.1021/acsami.6b02372.

58. J. Wang, H. Hu, L. Jia, et al., "Fast Interfacial Electrocatalytic Desolvation Enabling Low-Temperature and Long-Cycle-Life Aqueous Zn Batteries," *InfoMat* 6, no. 7 (2024): e12558, https://doi.org/10.1002/inf2.12558.

59. P. Qing, Z. Wu, A. Wang, et al., "Highly Reversible Lithium Metal Anode Enabled by 3D Lithiophilic–Lithiophobic Dual-Skeletons," *Advanced Materials* 35 (2023): 2211203, https://doi.org/10.1002/adma.202211203.

60. Y. Liu, X. Geng, M. Ma, et al., "In-Situ Modified Lithiophilic Layer Enriched With Multi-Alloys and LiF for Stable Lithium Metal Anode," *Journal of Alloys and Compounds* 1049 (2025): 185398, https://doi.org/10.1016/j.jallcom.2025.185398.

61. B.-I. Oh, Y. G. Jeon, and H.-K. Kim, "Lithiophilic–Lithiophobic Gradient Electrode for Dendrite-Suppressed Lithium Metal Anodes," *Journal of Energy Storage* 144 (2026): 119826, https://doi.org/10.1016/j.est.2025.119826.

62. N. Zhang, L. Du, J. Zhang, et al., "Self-Assembled Tent-Like Nanocavities for Space-Confined Stable Lithium Metal Anode," *Advanced Functional Materials* 33, no. 16 (2023): 2210862, https://doi.org/10.1002/adfm.202210862.

63. Y. Li, K. Yang, Z. Fan, et al., "Bilayer Artificial Interface Engineering Enables Dendrite-Free and Low-Temperature Stable Lithium Metal Batteries," *Energy Storage Materials* 83 (2025): 104664, https://doi.org/10.1016/j.ensm.2025.104664.

64. G. Zhang, J. Chang, L. Wang, et al., "A Monofluoride Ether-Based Electrolyte Solution for Fast-Charging and Low-Temperature Non-Aqueous Lithium Metal Batteries," *Nature Communications* 14, no. 1 (2023): 1081, https://doi.org/10.1038/s41467-023-36793-6.

65. Y. Liu, J. Shen, G. Hu, et al., "Stable Low-Temperature Lithium Metal Batteries With Dendrite-Free Ability Enabled by Electrolytes With Cooperative Li^+-Solvation," *Chemical Engineering Journal* 503 (2025): 158223, https://doi.org/10.1016/j.cej.2024.158223.

66. N. Piao, J. Wang, X. Gao, et al., "Designing Temperature-Insensitive Solvated Electrolytes for Low-Temperature Lithium Metal Batteries," *Journal of the American Chemical Society* 146, no. 27 (2024): 18281–18291, https://doi.org/10.1021/jacs.4c01735.

67. D. Guo, C. Xing, L. Chen, et al., "Upcycling FePO4 Residues From Spent Lithium-Ion Batteries Toward High-Rate $LiFePO_4$ Cathode by Constructing Hierarchical Conductive Frameworks," *Journal of Energy Chemistry* 110 (2025): 571–580, https://doi.org/10.1016/j.jechem.2025.07.016.

Supporting Information

Additional supporting information can be found online in the Supporting Information section.
Supporting Information S1: rar270388-sup-0001-suppl-data.docx.